First La2O2S infrared transparent ceramics

Alexandre Le Coz, Guillaume Durand, Louis Cornet, Nathalie Herbert, Françis Gouttefangeas, Loïc Joanny, Fabrice Célarié, François Cheviré, Odile Merdrignac-Conanec

First La_2O_2S infrared transparent ceramics

Alexandre Le Coz[a], Guillaume R. Durand[a], Louis Cornet[a], Nathalie Herbert[a], Francis Gouttefangeas[b], Loïc Joanny[b], Fabrice Célarié[c], François Cheviré[a], Odile Merdrignac-Conanec[a]*

[a] *Univ Rennes, CNRS, ISCR - UMR 6226, F-35000, Rennes, France*
[b] *Univ Rennes, CNRS, ScanMAT - UAR 2025, F-35000, Rennes, France*
[c] *Univ Rennes, CNRS, IPR - UMR 6251, F-35000, Rennes, France*

*Corresponding author: odile.merdrignac@univ-rennes1.fr

Abstract

Lanthanum oxysulfide (La_2O_2S) was investigated as infrared transparent ceramic to benefit from stronger chemical bonds and superior mechanical performances to that of non-oxide benchmark infrared materials. La_2O_2S ceramics were processed by hot-pressing powders prepared by combustion synthesis followed by a sulfurization treatment. Powders and ceramics were characterised through various techniques (XRD, UV-Vis-IR spectroscopy, particle size analysis, SEM, Impulse Excitation Technique, microhardness and fracture toughness tests) to assess their purity, study their microstructure and determine their optical and mechanical properties. The study reports the first IR transmission spectra, Poisson's ratio, Young's and shear moduli and fracture toughness values of La_2O_2S polycrystalline ceramics. The ceramics showed transparency in the 2-11 μm range and their mechanical performances were all superior to that of commercial infrared ceramics. The best transmission (89% of the theoretical transmission) was measured at 7.3 μm for 1 mm-thick ceramics hot-pressed at 1200-1250°C.

Key-words

La_2O_2S, hot-pressing, infrared transmission, Young modulus, Vickers hardness

1. Introduction

Since the discovery of the first highly-translucent Al_2O_3 ceramic ("Lucalox" from General Electrics) in 1959 [1,2] and the first polycrystalline $CaF_2:Dy^{2+}$ laser based on transparent ceramic in 1964 [3], tremendous research emerged on various transparent ceramics for different applications in passive or active optics, such as infrared (IR) windows/domes and transparent armors, or laser hosts, phosphors, scintillators and electro-optical components [4–7]. Optical transmission within a polycrystalline ceramic consisting of randomly oriented grains separated by grain boundaries is affected by diffusion phenomena from (i) the surface roughness (ii) the presence of pores or secondary phases having different refractive indices than the material and (iii) the grain boundaries in the case of birefringent materials, i.e. with an anisotropic refractive index. For the latter reason, a vast majority of transparent ceramics are derived from materials with isotropic lattice structure, i.e. cubic structure, in which the refractive index is constant regardless of crystal orientation, so that no scattering (refraction or reflection) occurs as light passes from grain to grain. In the case of non-cubic crystal structures, scattering theories indicate that reduction of the grain size down to the submicrometric range drastically minimizes birefringence-related light loss [8–10]. Indeed, it has been reported that the in-line transmission of polycrystalline alumina ceramic (hexagonal) is significantly increased for small mean grain sizes (1–2 μm) [9–11] and that a remarkable transparency is observed for 0.5 μm mean grain size [8,12]. Besides optical performances, very fine-grained microstructures with submicrometric grain sizes are also beneficial to achieve components with improved hardness, wear resistance and strength [13]. In order to produce fine-grained and fully dense ceramics, fine precursor powders (nanometric size for non-cubic materials) with high chemical purity (>99%) and homogeneity of green bodies are some of the required features [4,12,14–16].

This study reports the processing of lanthanum oxysulfide (La_2O_2S)-based transparent ceramics and the evaluation of their performances as IR windows. La_2O_2S is widely studied as an efficient luminescent host matrix on the basis of its low phonon energy, good chemical stability and low toxicity [17–20]. However, little research has been conducted on this ceramic compound as a transparent bulk material. Yet, in addition to the above mentioned physico-chemical properties, La_2O_2S has a high melting point and a high density making feasible the production of transparent ceramics by sintering techniques. To the best of our knowledge, the processing of translucent La_2O_2S ceramics has only been reported twice in literature [21,22], but no transmission value in the visible range nor in the infrared were reported. The fact that optical transparency of bulk La_2O_2S has not attracted much interest until now probably stems, as stated above, from the lesser interest in non-isotropic crystalline structures, unlike ZnS (blende structure) known both as phosphor for over 100 years [23] and as bulk ceramic for infrared windows [24,25]. With the presence of sulfur atoms, La_2O_2S transparency window lies between that of oxides like alumina and that of pure sulfides like ZnS. The emergence of non-oxide polycrystalline ceramics arose indeed from the need to extend the transparency domain of polycrystalline materials to the far infrared. Today, ZnS, the reference material for applications in the 3-5µm and 8-12µm infrared atmospheric windows [26,27], is produced under the trademarks FLIR® and Multispectral® by long and complex processes (Chemical Vapor Deposition and Hot Isostatic Pressing) which lead to expensive optics. For application as external structural windows able to withstand harsh environments, ceramic materials should combine mechanical strength, erosion resistance and elevated temperature performance. Durable protective coatings are generally necessary for such external use in severe environment [28]. The development of new products like La_2O_2S could satisfy the important needs for materials with extended transparency in the infrared (compared to oxides) and superior robustness (compared to sulfides) towards harsh environments.

La_2O_2S and more generally R_2O_2S (R=rare earth element) compounds are conventionally prepared through a solid-state reaction assisted or not by a flux agent [17,29–33]. Reduction of rare-earth oxysulfates under hydrogen-helium mixture or sulfurization of rare-earth oxides or other precursors (e.g. carbonates) under H_2S, CS_2 or S vapor can also lead to R_2O_2S [34–36]. However, to produce fine powders, methods involving lower temperatures and small-term annealing times are required. In this study, a combustion synthesis technique was preferred over other liquid phase methods (e.g. gel-network coprecipitation method [37], sol-gel polymer thermolysis [38] or solvothermal pressure-relief process [39]) for its shorter reaction times and its efficiency in producing fine and well-crystallized La_2O_2S powders [18,19,40–42].

Powder synthesis and powder sintering as well as the techniques used to characterise powder and ceramic samples are presented first. Then powders and ceramics are successively characterised in terms of purity and morphology/microstructure and optical transmission and mechanical properties of La_2O_2S ceramics are compared to that of common infrared transparent ceramics. Finally, correlation between the degree of optical transmission or hardness of the ceramics and their characteristics (porosity, grain size) is clearly established and deeply discussed.

2. Experimental

2.1. Powder synthesis

La_2O_2S powders were prepared by the solution combustion method following the procedure described in previous work [19]. The starting materials, $La(NO_3)_3$, $6H_2O$ (Alfa Aesar, 99.99%) and thioacetamide (TAA) CH_3CSNH_2 (ACROS organic, 99+%), were dissolved in absolute ethanol (Prolabo, VWR Chemicals) under magnetic stirring at ~70°C. A fuel (TAA)/oxidant (lanthanum nitrate) molar ratio of 60:11 was used in all preparations. The solution was then introduced into a muffle furnace (Nabertherm GmbH L40/11/B410) pre-heated to 500°C. The white foam obtained was subsequently ground before post-sulfurization.

A homogeneous 20 g batch of as-combusted powders was prepared by mixing 5 consecutive batches (approx. 4 g each) with a WAB rotary mixer - TURBULA® Type T2C. The sulfurization treatment was carried out in an oscillatory reactor tube furnace (HTR Carbolite Gero) under H_2S/N_2 (10/90) flow at 1000°C for 6 h.

2.2. Powder sintering by Hot Pressing

Hot Pressing was carried out under dynamic vacuum (about 0.3 - 0.4 mbar) using VAS (France) equipment. A typical quantity of 2.3 g of powder was introduced in a 13 mm diameter graphite die coated beforehand with boron nitride BN (Alfa Aesar 99,5 %) to facilitate demolding. Powders were sintered at 1100°C, 1200°C, 1250°C, 1300°C, 1350°C and 1400°C with a heating rate of 10°C/min. A load of 120 MPa (maximum pressure allowed on graphite die) was applied at the selected sintering temperature (1100-1400°C) for a 2-hour dwell time. At the end of the dwell time, the pressure was released and samples were cooled to 1000°C at a rate of 4°C/min, then naturally cooled down to room temperature. The ceramics were optically polished with a final step using 0.1 µm alumina powder prior to transmission measurements.

2.3. Characterisation techniques

X-ray diffraction (XRD) patterns were recorded at room temperature in the 5-90° 2θ range with a step size of 0.0261° and an effective scan time per step of 40 s using a PANalytical X'Pert Pro diffractometer (Cu-L2,L3 radiation, λ = 1.5418 Å, 40 kV, 40 mA, PIXcel 1D detector). Data Collector and HighScore Plus softwares were used respectively to record and analyse the diffractograms. The XRD patterns for Le Bail structural refinements were collected at room temperature in the 5-120° 2θ range with a step size of 0.0131° and an effective scan time per step of 200 s. All calculations were carried out with Fullprof and WinPLOTR programs [43,44]. The Thompson-Cox-Hastings pseudo-Voigt (NPr = 7) convoluted with axial divergence asymmetry function and gaussian approximation were used and the background was approximated by linear interpolation between a set of background points. The $P\bar{3}m1$ (#164) space group and lattice parameters: a = b = 4.05 Å, c = 6.94 Å, $\alpha = \beta = 90°$ and $\gamma = 120°$ were used as input data (COD card n°96-210-6403) [45].

A Gemini VII 2390 Micromeritics analyzer was used to determine the specific surface area (SSA) of the powders by the Brunauer-Emmett-Teller method. Before measurement, the samples were outgassed overnight in vacuum at 250 °C.

Particle size distribution analysis of the powders was performed with a Laser Particle Sizer Analysette 22 NanoTec (FRITSCH GmbH). Powders were dispersed in water and ultrasonicated during analysis. Scanning Electron Microscopy (SEM) for powders morphology and ceramics microstructure analyses was performed using a JEOL JSM 7100 F[1]. Prior to SEM observations, the samples were metallized with carbon. Particle size of the powders was also estimated from SEM images via the ImageJ software. Grain boundaries of the ceramics were revealed by thermal etching at 1010°C for 30 min in H_2S/N_2 flow. SEM observations of the thermally etched samples were then used to determine the grain size from about 100 to 400 grains via ImageJ.

Fourier Transform Infra-Red (FTIR) patterns of powders samples dispersed in KBr pellets were recorded at room temperature with a Nicolet 380 FT-IR spectrometer (Thermo Electron Corporation) between 400 and 4000 cm^{-1}. Diffuse reflectance spectra of powders samples were collected using a Varian Cary 100 Scan spectrometer equipped with a Varian WinUV software and the integrating sphere Lab-sphere (DRC-CA-30). Experimental data were collected within the 200-800 nm range with a 1 nm step. Band gap of the material (E_g) was calculated using the Tauc plot generated from Kubelka-Munk data in the case of an allowed indirect transition [46,47]. The transmission spectra of the ceramics samples were recorded with a Bruker T37 infrared spectrometer between 400 and 8000 cm^{-1}.

The density of the sintered samples was measured by Archimedes method in absolute ethanol with a precision of about 1 %. The relative density (or densification rate) of the ceramics was estimated using a calculated density of 5.750 $g.cm^{-3}$ computed from the refined lattice parameters which is in good agreement with the La_2O_2S density value of 5.76 $g.cm^{-3}$ from the COD card n°96-210-6403 [45]. Vickers microhardness (H_v) and resistance to crack propagation (fracture toughness, K) measurements were performed on polished ceramic surfaces using a Matzusawa MXT 70 Microhardness tester with 200 gf and 10 sec test load and time, respectively. Vickers

[1] At Centre de Microscopie Electronique à Balayage, CMEBA facilities (UAR 2025 ScanMAT)

microhardness and fracture toughness are median values determined on 8 indents. The Vickers imprint diagonals and cracks length were measured using a digital KEYENCE VHX-5000 microscope. The indentation fracture toughness K (MN.m$^{-3/2}$) was computed using Niihara *et al.* equation [48] with $0.25 \leq l/a \geq 2.5$, proposed in the case of a Palmqvist crack propagation model [49] :

$$K = 0.0089\left(\frac{E}{H_v}\right)^{2/5}\frac{P}{a\sqrt{l}}$$

H_v is the Vickers hardness (N.mm^{-2}), P the applied load (MN), l the average Palmqvist crack length (m), a the average length of the indent half diagonal (m) and E the Young's modulus of the material (N.mm^{-2}).

The Young's modulus *E* and shear modulus *G* were obtained at room temperature with an impulse excitation technique (IET) (RFDA, IMCE, Belgium) [50]. The sample was suspended on wires at the nodes of the first torsion vibration mode. The sample was impacted by a small ceramic projectile in free fly and the vibration signal was recorded by a microphone (sampling rate 250 kHz) and processed with the RFDA software. From the bending vibration frequency and the shear vibration frequency, Young's modulus and shear modulus were calculated according to the equation proposed in ASTM E 1876 [51].

3. Results

3.1. Powder characterisation

XRD patterns of as-combusted and post-sulfurized powders are presented in Fig. 1. After combustion, the powders readily contain La_2O_2S as the main phase with traces of $La_2O_2SO_4$ (ICCD card n° 00-041-0678) as secondary phase. The latter is eliminated after the 6-hour sulfurization treatment. All the powders are identified as hexagonal La_2O_2S (space group $P\bar{3}m1$) according to the COD card n° 96-210-6403.

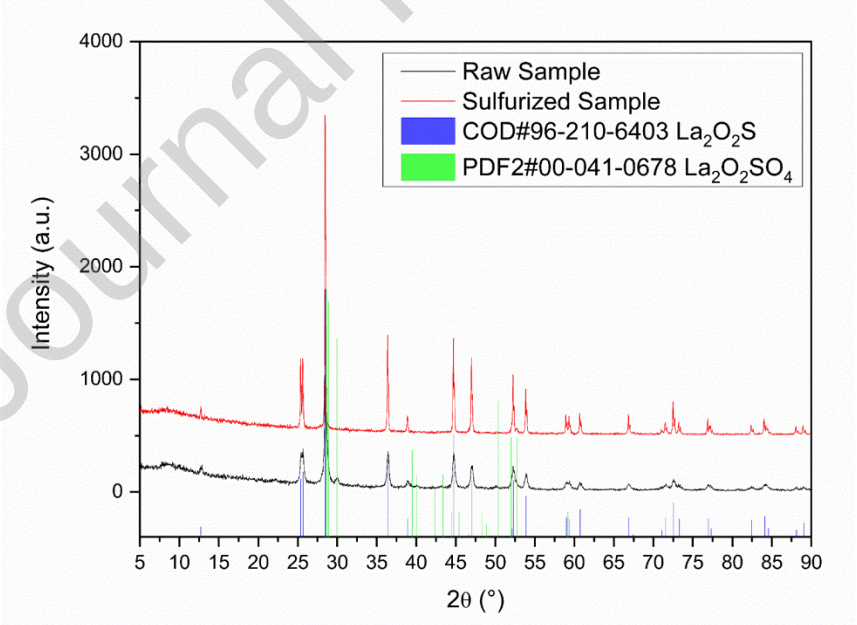

Fig. 1. X-ray diffraction patterns of as-combusted and pure (sulfurized) La_2O_2S powders

The lattice parameters and average crystallite sizes of the powder samples were estimated by Le Bail refinement. The final refinement pattern of La_2O_2S powder is presented in Fig. 2. The resulting unit cell parameters (a = b = 4.052 Å ; c = 6.946 Å) are in close agreement with the literature [45]. The low values of figures of merit certify the validity of the refinement model. The heat treatment at 1000°C for 6 h induces a magnification of the crystallite size as evidenced with the decrease of the Full Width at Half Maximum (FWHM) of XRD peaks. The average crystallite sizes were determined to be 27.8 nm and about 168 nm for the as-combusted and sulfurized powders, respectively.

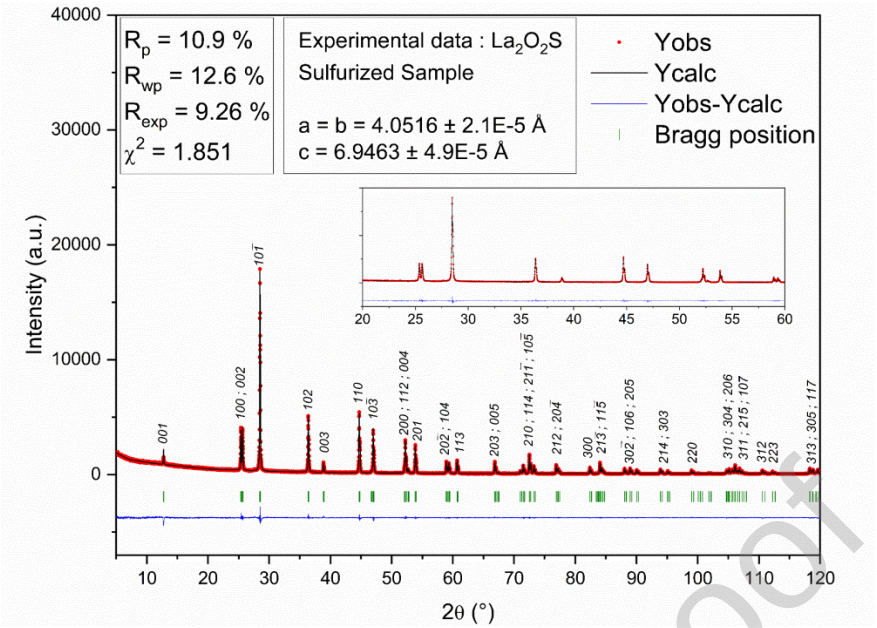

Fig. 2. Final Le Bail refinement of pure La_2O_2S (sulfurized) powder

Fourier Transform Infra-Red (FTIR) spectroscopy was used to further assess the purity of the powders (Fig. 3). Indeed, impurities at traces levels in ceramics induce absorption bands that are detrimental to the transmission, especially sulfate species whose absorption bands lie in the infrared region of interest. The as-combusted powders actually contain several absorption peaks between 600 cm^{-1} and 4000 cm^{-1}. The relatively strong absorption bands at 3300-3610 cm^{-1} and the weak peak located at 1630 cm^{-1} are characteristic of symmetric ν_1 and antisymmetric ν_3 stretching modes and bending ν_2 mode of H_2O [52,53]. The two absorption bands at 560-700 cm^{-1} and 1000-1250 cm^{-1} are attributed to ν_1, ν_3 and ν_4 stretching modes of sulfate groups, due to the presence of the $La_2O_2SO_4$ secondary phase [54] identified by XRD. These vibration bands weaken after sulfurization as the residual oxysulfate is converted into La_2O_2S which is consistent with XRD results. Two additional absorption bands located at around 1350-1580 cm^{-1} are attributed to carbonate groups adsorbed on La_2O_2S surface originating from the chemisorption of CO_2 released by TAA decomposition [20,55,56]. All these peaks decrease significantly after sulfurization (1000°C for 6h). The bands centred at 400-550 cm^{-1} are characteristic La−O and La−S vibrational bands of La_2O_2S [57]. These results confirmed the high purity of the sulfurized powder.

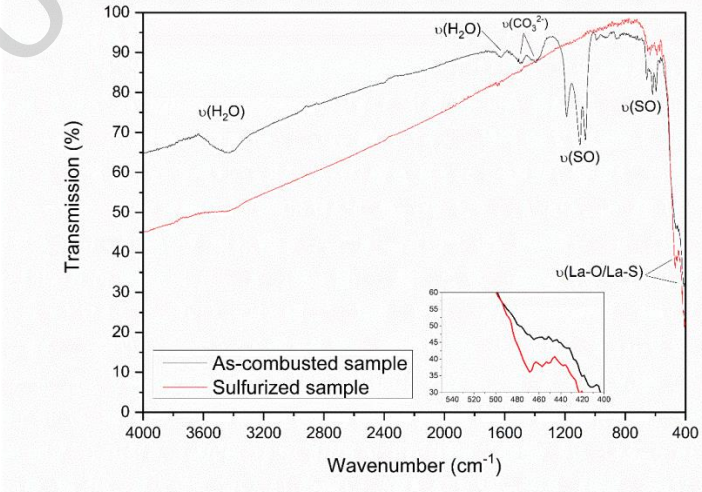

Fig. 3. FTIR analysis of as-combusted and pure La_2O_2S powders. In insert: zoom on the 460 cm^{-1} peak associated to the La-O/La-S bonds

Fig. 4 shows the diffuse reflectance spectrum of the La_2O_2S powders. A drastic drop in reflection is observed in the UV range in consistency with the white colour of the powder. This reflection loss is attributed to free carrier absorption above the band gap which is estimated to be 3.75 eV by the Tauc method. This result is in good agreement with the value reported by Sobon *et al.* who determined on La_2O_2S single crystals a UV cut-off of 350 nm corresponding to a band gap of 3.54 eV [58].

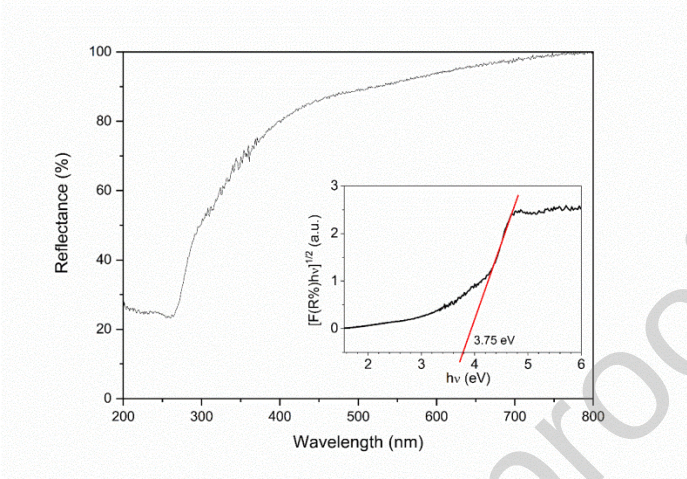

Fig. 4. Diffuse reflectance spectrum of La_2O_2S powder and band gap (E_g) Tauc plot

SEM micrographs of the as-combusted and sulfurized samples are compared in Fig. 5. Both powders are made up of agglomerates of different size lying in the range from a few microns to a few tens of microns. The high magnification images (Fig. 5(b)(d)) reveal differences in primary particles morphology in consistency with the compositional heterogeneity. While the as-combusted powder is made of primary particles that are heterogeneous in shape (plate-like or rounded) and size (micrometric or nanometric, respectively), the sulfurized powder is made of primary particles of uniform rounded shape and homogenous nanometric size (60-380 nm with median size of 136 nm, determined via ImageJ). The heat treatment at 1000°C in H_2S/N_2 finally leads to an interconnected morphology, arising from the formation of necks between primary particles, which is typical of the initial stage of solid-state sintering. As a result, the SSA of the pure powders is significantly reduced (4 $m^2.g^{-1}$) in comparison with the as-combusted powders (12 $m^2.g^{-1}$).

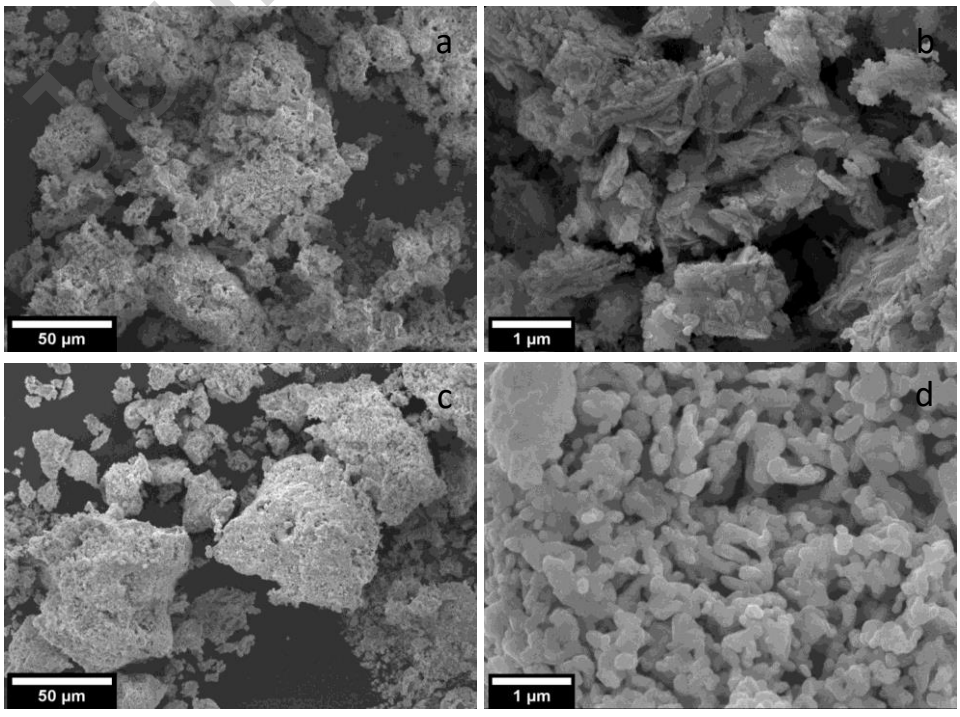

Fig. 5. SEM images of (a,b) as-combusted and (c,d) sulfurized powder (pure La_2O_2S)

The particle size distribution of the pure La_2O_2S powders has been measured by laser granulometry (Fig. 6). The latter shows a large unimodal size distribution centered at 30 µm with a small distribution tail extending from 5 µm to the submicrometric range. These results are consistent with SEM images showing both agglomerates of a few tens of microns (Fig. 5(c)) and rounded primary particles of nanometric size (median size of 136 nm) (Fig. 5(d)). The average particle diameter (d_{BET}) determined to be 281 nm from the measured SSA and the calculated density (5.750 $g.cm^{-3}$) on supposedly spherical non-porous particles fits rather well the SEM particles size if we consider this value is overestimated as the particles are actually partially sintered.

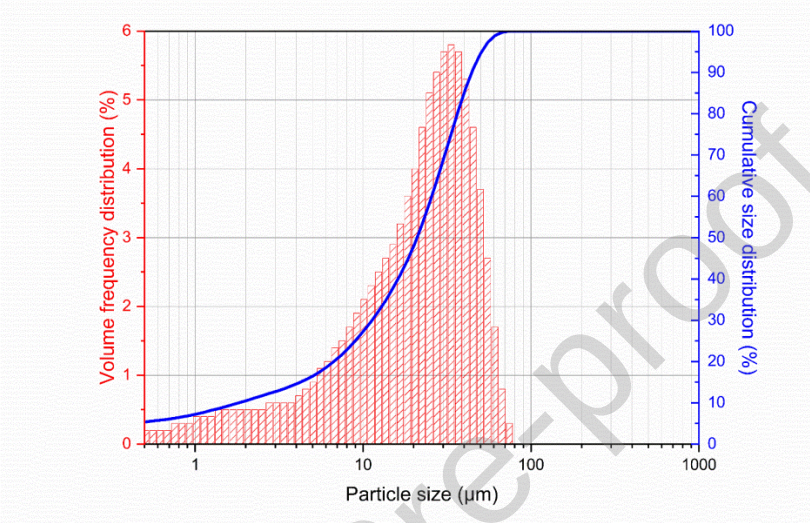

Fig. 6. Particle size and cumulative size distributions of La_2O_2S powders in the 1000-0.5 µm range (Franhaufer theory limit)

3.2. Ceramics characterisation

The XRD patterns of the hot-pressed La_2O_2S ceramics are similar and comparable to that of the precursor powder so that only the pattern of the sample sintered at 1250°C is presented in Fig. 7. Refined unit cell parameters (median value on the temperature range 1100-1400°C, a = b = 4.0515 ± 5E-5 Å; c = 6. 9479 ± 9E-5 Å) are similar to that of the precursor powder. Le Bail refinement results are gathered in supplementary information. It is noteworthy to mention that EDX analyses indicate that the S/La ratio remains constant for all the processed ceramics (see Supplementary Information, Table S1).

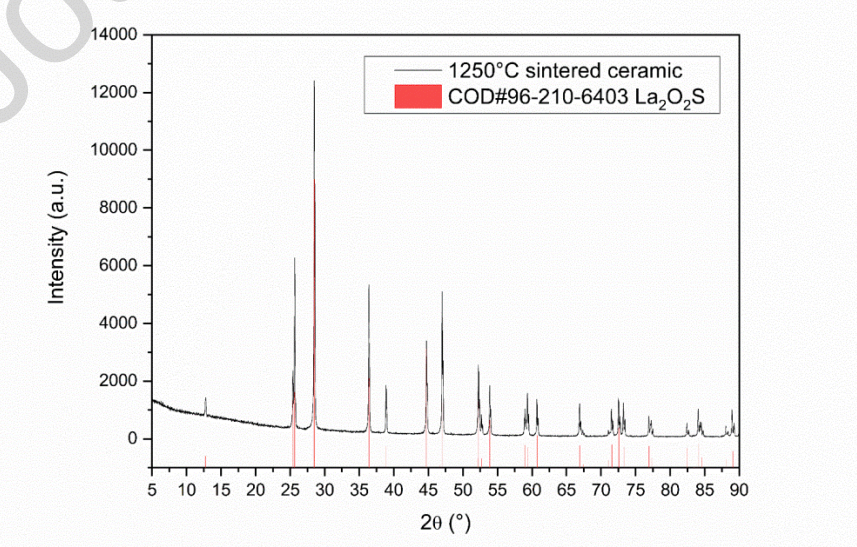

Fig. 7. X-ray diffraction pattern of La_2O_2S ceramic hot-pressed at 1250°C

The ceramics were all sintered to a relative density ≥ 99%. The SEM micrographs of thermally etched surfaces of La_2O_2S ceramics show residual closed porosity, characteristic of the final stage of sintering in agreement with the densification rate (Fig. 8). This porosity appears mainly at grain boundaries with size varying from nanometer (< 50 nm) to micrometer scale (> 0.4 µm) for sintering temperatures lower and higher than 1250°C respectively. Moreover, as expected with sintering process, an increase in grain size is observed with higher sintering temperature. Fig. 9 shows that the variation in pore size and grain size with sintering temperature is similar and presents the same turnover at around 1200-1250°C as highlighted by the linear fit.

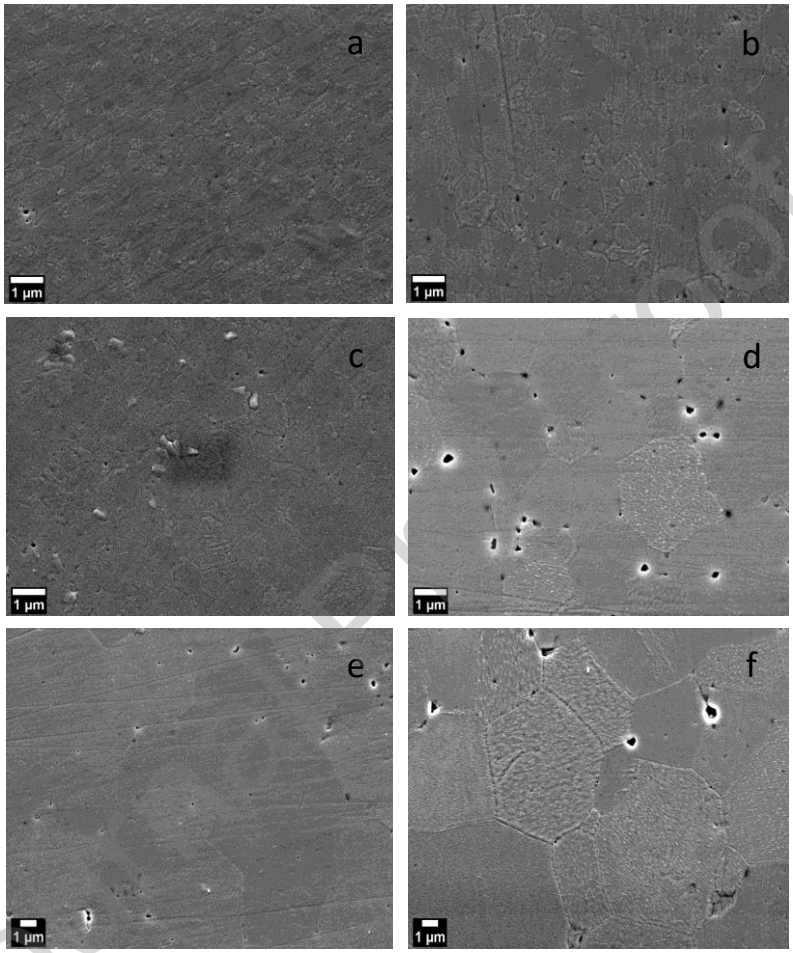

Fig. 8. SEM images of thermally etched surfaces of La_2O_2S ceramics hot-pressed for 2 h at (a) 1100°C (b) 1200°C (c) 1250°C (d) 1300°C (e) 1350°C and (f) 1400°C. Note the lower magnification employed for grains visualization in Figs. (e) and (f)

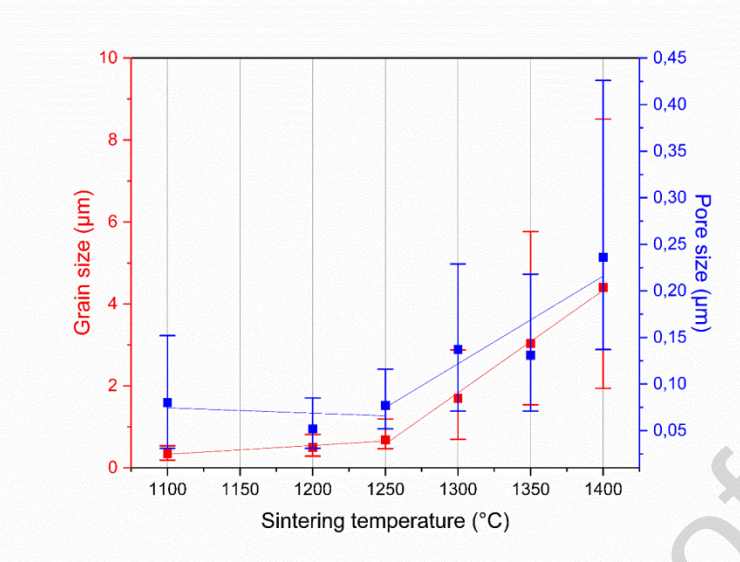

Fig. 9. Grain size (left) and pore size (right) of La_2O_2S ceramics as a function of sintering temperature. Error bars correspond to the percentile values d10 and d90.

Fig. 10 presents the IR transmission spectra of the La_2O_2S ceramics hot-pressed for 2 h at temperatures from 1100°C to 1400°C and a photograph of the ceramic hot-pressed at 1250°C. Note that these spectra are the first reported transmission data of polycrystalline La_2O_2S ceramics. The high wavelength cut-off (multiphonon cut-off around 10.9 µm) corresponds to the absorption due to lattice vibrations, in particular that due to La-O bonds (here, second harmonic vibrations) whose fundamental vibration was evidenced at around 460 cm^{-1} in the FTIR powder spectrum (Insert Fig. 3). At low wavelengths, the transmission is mostly altered by scattering due to microstructure defects. No absorption band is observed in the whole transparency window proving our La_2O_2S ceramics are highly pure. The transmission level of the ceramics depends on their sintering temperature. A maximum of 67% transmission is obtained at λ = 7.3 µm for 1 mm-thick ceramics sintered at 1200°C and 1250°C (overlapping spectra). This transmission represents 89% of the theoretical level (75.3%) determined from a La_2O_2S refractive index of 2.2 [59–61]. When the thickness is reduced to 0.5 mm, the ceramic exhibits some translucency as shown in Fig. 11 (see Supplementary Information for transmission spectrum).

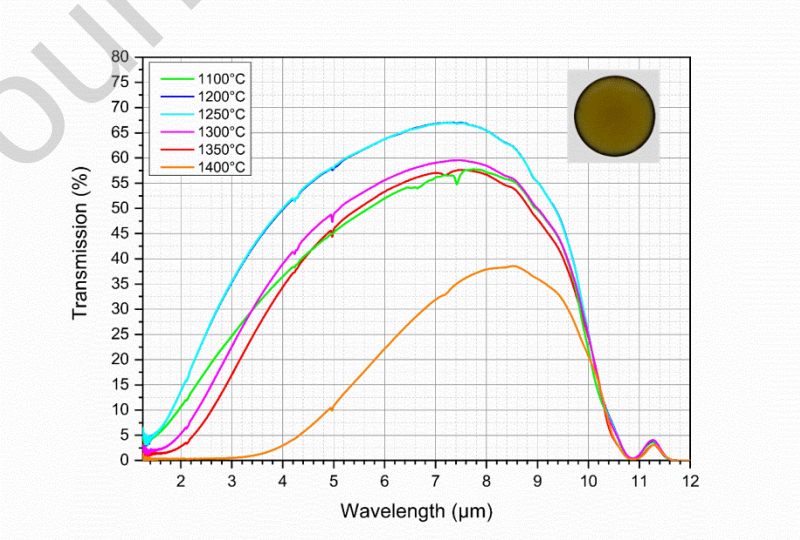

Fig. 10. IR transmission spectra of La_2O_2S ceramics hot-pressed in the temperature range 1100-1400°C (Thickness = 1 mm) and photograph of sample sintered at 1250°C (dark edge due to the hot-press graphite die)

Fig. 11. Photograph of La_2O_2S translucent ceramic sintered at 1250°C (Thickness = 0.5 mm)

Young's and shear moduli, Poisson's ratio and Vickers hardness of the hot-pressed La_2O_2S ceramics are reported respectively in Table 1 and Fig. 12. As expected from the nature of chemical bonds, Young's modulus and Vickers hardness of La_2O_2S are superior to that of common non-oxide infrared transparent materials like ZnS, ZnSe or CaF_2 (Table 2). For example, hardness values of about 550 $kgf.mm^{-2}$ obtained for the ceramics exhibiting the best transmission (hot-pressed at 1200 °C and 1250 °C) are three times and about four times greater than those of CVD ZnS (Standard or FLIR®) and CVD/HIP ZnS (Multispectral® or Clear®), respectively.

Table 1. Young's and shear moduli and Poisson's ratio of La_2O_2S ceramics hot-pressed at 1250°C (∅20 mm)

	Young's modulus (GPa)	**Shear modulus (GPa)**	**Poisson's ratio**
Calculated value	138.0 ± 2	53.4 ± 0.8	0.29 ± 0.01

Furthermore, as seen from Fig. 12 representing the evolution of ceramics hardness and grain size as a function of sintering temperature, hardness decreases with grain size following a two-stage regime either side of 1250°C.

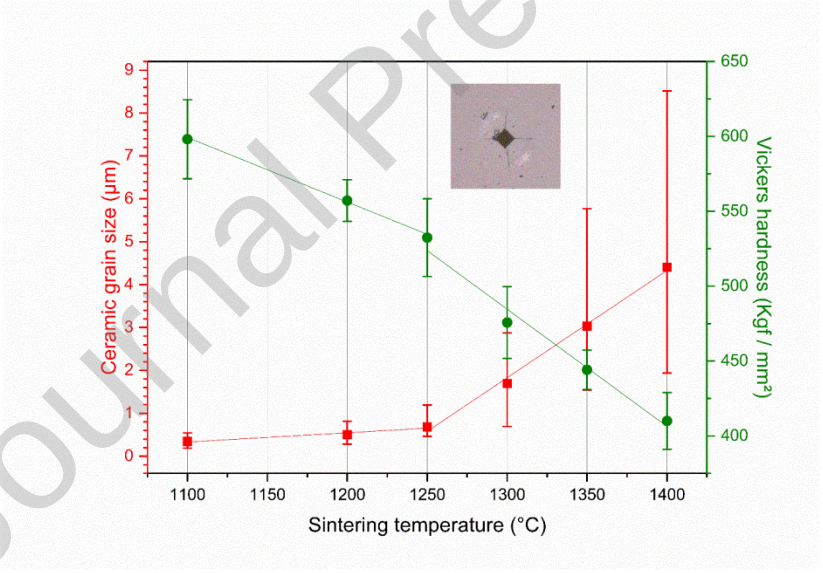

Fig. 12. (a) Median grain size (d50) (left) and Vickers hardness (right) of La_2O_2S ceramic as a function of sintering temperature (b) Micrograph of Vickers indentation pattern in La_2O_2S ceramic hot-pressed at 1200°C. Error bars correspond to (left) the grain size percentile values d10 and d90 and (right) the standard deviation of Vickers hardness values

Table 2. Vickers hardness, Young's modulus and Poisson's ratio values of common infrared transparent ceramics

Material	**Processing**	**Vickers hardness H_v ($Kgf.mm^{-2}$)**	**Young's modulus (GPa)**
FLIR® CVD ZnS (Vitron) [62]	CVD	178.3	74
Clear® CVD ZnS (Vitron) [62]	CVD + HIP	148.3	88
ZnS-ISCR [63]	Hot Pressing	310	85.9
ZnSe (APC) [64]	CVD	112	67.2
CaF_2 [65,66]	Single crystal	170	110
$CaLa_2S_4$-ISCR [67,68]	Hot Pressing	570	95.8

Table 3 presents the fracture toughness K of the ceramics determined using the Palmqvist cracks propagation model [49], along with their grain size and sintering temperature. It appears clearly that the ceramics have similar fracture toughness values (mean value: 1.01 $MN.m^{-3/2}$) and that the grain size, in the range 0.3-4.4 µm, has no influence on fracture toughness.

Table 3. Fracture toughness K (Vickers indentation) and grain size of La_2O_2S ceramics hot-pressed in the temperature range 1100-1400°C

Sintering temperature (°C)	Fracture toughness K* ($MN.m^{-3/2}$)	Median grain size (µm)
1100°C	1.01 ± 0.07	0.346
1200°C	0.93 ± 0.02	0.502
1300°C	1.05 ± 0.19	1.695
1350°C	0.96 ± 0.07	3.034
1400°C	1.03 ± 0.10	4.406

*Niihara model (see 2.3. experimental section)

4. Discussion

In this work, we report the processing, mechanical properties and optical transmission spectra of the first infrared transparent La_2O_2S ceramics by providing to the best of our knowledge the first transmission spectra of La_2O_2S-based ceramics attesting for transparency in the 2-11 µm infrared range.

First, XRD data, FTIR and UV-Visible spectroscopy prove that highly pure La_2O_2S powders are synthesized by combustion method and post-sulfurization in H_2S/N_2 flow. Results of crystal lattice refinements using the Le Bail method are in agreement with literature data.

Laser granulometry analysis of La_2O_2S powders shows a rather large unimodal particle size distribution in the micrometric range, centred at 30 µm. SEM observations reveal that powders are in fact made up of micrometric agglomerates constituted of nanometric primary particles. The median primary particle size (136 nm) can directly be correlated to the average crystallite size (168 nm) determined from peak broadening by Le Bail refinement. Thus, we can assume that each primary particle of powder is on average composed by one crystallite. We observed also that the thermal treatment associated to the sulfurization process induced a partial sintering of the particles which is presumably facilitated by the agglomerated morphology of the as-combusted powder. This is corroborated to the SSA value (4 $m^2.g^{-1}$) where a value about double (8 $m^2.g^{-1}$) would be expected for a perfect unagglomerated powder made up of primary dense and spherical particles of 136 nm, using the Brunauer-Emmett and Teller model [69]. However, the powder morphology did not impede its sinterability as 99% densification was reached in 2-hour hot pressing. Microstructural characterisations of the ceramics (Fig. 8(d)(e)(f)) exhibit a decisive turn in the 1200-1250°C temperature range in terms of grains and pores size as shown by the slope change of the tendency curves in Fig. 9. Indeed, an increase in grain size (as well as in pore size) with increasing sintering temperature occurs to a large extent (by a factor of 6) between 1250 and 1400°C (Fig. 9).

IR transparency is to be related to the ceramics microstructure. We observed a significant increase in transmission from 1100°C up to 1200-1250°C while beyond 1250°C, IR transmission is lowered (Fig. 10). As no correlation from the sintering temperature with the densification rate was noticed, we associate the transmission variation to the pore size evolution. For sintering temperatures below 1250°C, one note a pore size homogenization at 1200°C and 1250°C compared to 1100°C (Table S2 in Supplementary Information) leading to fewer large pores, thus limiting light scattering phenomenon at low wavelengths. For sintering temperatures above 1250°C, a decrease in transmission is clearly observed with increasing temperature which ends up being drastic at 1400°C. SEM analyses show indeed an increase in the number of intragranular pores at high sintering temperature (>1250 °C) testifying of what could be the beginning of abnormal grain growth. This type of growth occurs when the pores mobility is too low compared to that of grain boundaries so that pores separate from the latter. It leads to an exaggerated growth of some grains to the

detriment of the small ones that explains the increasing deviation from the d_{10} to the d_{90} grain size values for sintering temperatures above 1250 °C. It seems that if sintering was driven by diffusion at grain boundaries and growth limited by grain boundaries mobility for sintering temperatures below 1250 °C, it is no longer the case when exceeding 1250 °C. We can assume that the grain boundaries mobility increase is associated to a change in the sintering mechanism being mainly due to volume diffusion at grain boundaries with grain boundaries-pores separation at high temperature [70]. Moreover, a significant increase in pores size is observed with increasing temperature. Some pores of about 500 nm are observable at 1300°C while at 1400°C some are micrometric. At this stage, two hypotheses can be formulated regarding the pore size growth, one not excluding the other:

(i) One can fairly imagine that the abnormal grain growth is accompanied by a pore growth due to the coalescence of the latter.

(ii) The increase in pore size may result from the fact that the pressure is applied at the sintering temperature and not from the beginning of the sintering process. One can assume that for the highest temperatures (1300-1400°C), the pressure is applied onto agglomerates that have already started to sinter, leaving by shrinkage, large inter-agglomerate cavities from which the large pores result (Fig. 13).

In both cases, as light wavelength approaches the pore size, scattering effect increases and transmission decreases [26]. As a result, the lower limits of the transparency window and the transmission maximum are both shifted to higher wavelengths. It is to be noted that, at 1400°C, sintering produces, as observed from SEM images (Fig. S7), a small proportion of large pores (> 1µm) that are responsible for the important shift of the transparency window at this temperature. Note that diffusion due to birefringence shall not be considered as a source of optical losses in our samples. Indeed, refractive indices of La_2O_2S are close enough (< $1x10^{-2}$ at 1 µm [58]) to neglect birefringence effect at grain boundaries when compared to diffusion phenomenon associated to the residual porosity.

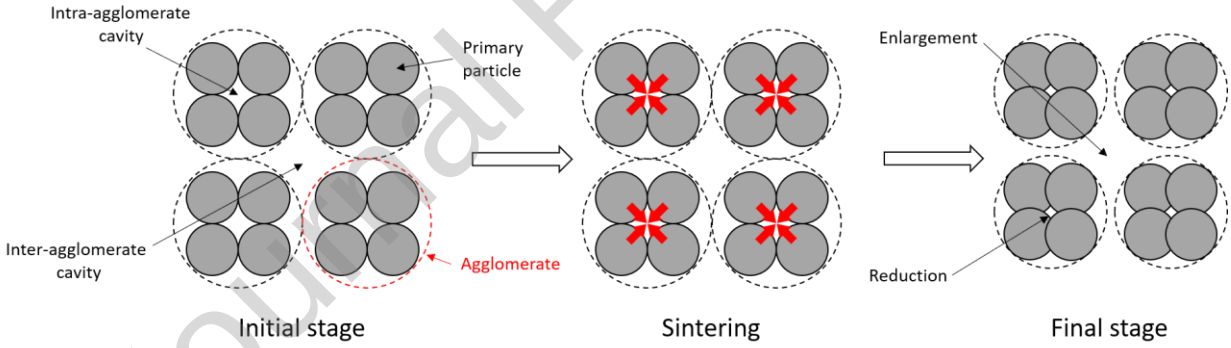

Fig. 13. Schematic of differential sintering

Hardness measurements revealed decreasing values with increasing sintering temperatures from about 600 to 400 $kgf.mm^{-2}$ (Fig. 12). They exhibit, as in Fig. 9, a decisive turn in the 1200-1250°C temperature range, shown by the slope change of the tendency curves. This behaviour is explained by the abnormal grain growth which operates above 1250°C. Moreover, La_2O_2S hardness increases inversely with the square root of the grain size, testifying of a Hall-Petch behaviour which is attributed to dislocation pile-ups at grain boundaries (limited dislocation mobility in smaller grains) (Fig. 14) [71,72]. Finally, hardness of the samples with the best transparency is about three times greater than that of commercial CVD ZnS and when compared to hot-pressed ZnS and $CaLa_2S_4$ from our previous studies, is about twice that of ZnS and comparable to that of $CaLa_2S_4$ (Table 2).

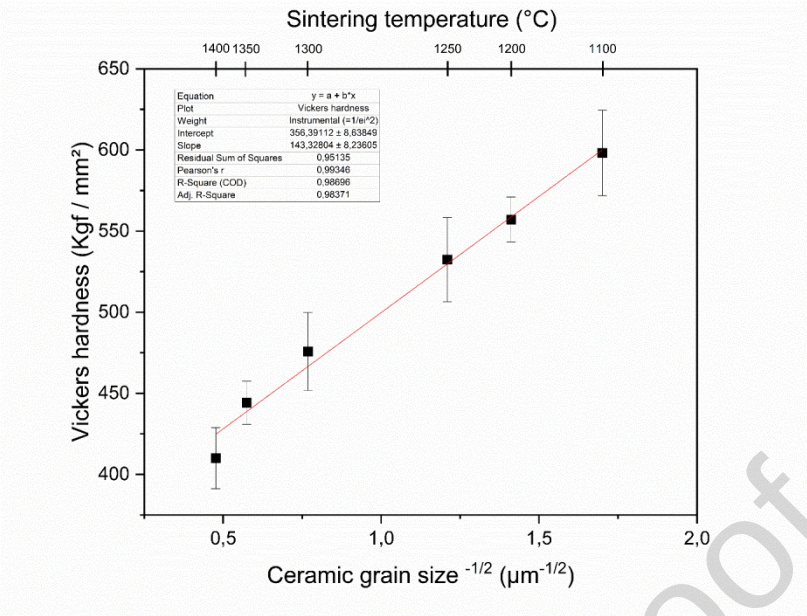

Fig. 14. Vickers hardness as a function of (grain size)$^{-1/2}$ of La_2O_2S ceramics hot-pressed at temperatures in the range 1100-1400°C

As mentioned earlier, the fracture toughness of all tested La_2O_2S samples is about 1.01 MN.m$^{-3/2}$. The independence of fracture toughness on grain size is often reported for cubic materials and non-cubic fine-grained alumina [73,74]. Indeed, for alumina ceramics with grains size comprised between several hundred nanometers up to a few microns, the toughening mechanism usually reported as crack bridging (i.e. formation of a strong reinforcing phase that connects the two crack surfaces in the form of whiskers, continuous fibres or elongated particles [75]) can not be effective. We assume in our non-cubic La_2O_2S ceramics with median grain sizes in the range 0.3-4.4 µm a similar behaviour to occur. As a result, the measured fracture toughness (Table 3), as grain size independent, can be considered as the true intrinsic material toughness.

5. Conclusion

In this work, we report the processing and the first optical and mechanical properties of La_2O_2S-based infrared transparent ceramics. La_2O_2S powders were synthesized by combustion method and sulfurization in H_2S/N_2 (10/90) gas flow at 1000°C and subsequently hot-pressed for 2 h under 120 MPa in the temperature range 1100-1400°C. La_2O_2S powders made up of agglomerates (~ 30 µm) of nanometric particles (~ 136 nm) were densified to a relative density over 99% in only 2 h by hot pressing. Optical transmission is highly dependent on the ceramics microstructure showing limited grain growth (0.3-0.7 µm) at lower sintering temperatures (1100-1250°C) followed by abnormal grain growth (1.7-4.4 µm) at higher temperatures. Young's modulus and Vickers hardness are superior to that of any commercial infrared transparent ceramics and are, in particular, 2 times higher and 3 times higher to that of CVD ZnS, respectively. Hardness is closely related to the grain size showing a moderate decrease while the grain size remains fairly constant for ceramics hot pressed between 1100°C and 1250 °C, and a larger decrease for ceramics hot pressed at 1300-1400°C which undergo abnormal grain growth. The maximum of transmission observed at 7.3 µm is reached for samples sintered at 1200°C and 1250°C with a value of 67 % (89% of theoretical transmission). Future improvements in powder morphology (deagglomeration) are promising prospects to achieve higher transmission values at low wavelengths, especially in the 3-5 µm atmospheric window. Such polycrystalline transparent La_2O_2S hot-pressed ceramics are believed to be promising candidates for transparent windows in harsh environment.

Acknowledgements

The authors are grateful to the French Direction Générale de l'Armement (DGA) and the Ministère des armées - Agence de l'Innovation de Défence (AID) for their financial support.
The authors are also thankful to Tanguy Rouxel and Alexis Duval at l'Institut de Physique de Rennes (IPR) UMR 6251 CNRS, for their expertise regarding fracture toughness and mechanical properties evaluation.

References

[1] R.L. Coble, Preparation of transparent ceramics Al_2O_3, American Ceramic Society Bulletin. (1959) 38507.

[2] R.L. Coble, Transparent Alumina and Method of Preparation, US Patent N°3026210, 1962.

[3] S.E. Hatch, W.F. Parsons, R.J. Weagley, HOT-PRESSED POLYCRYSTALLINE CaF_2:Dy^{2+} LASER, Appl. Phys. Lett. 5 (1964) 153–154. https://doi.org/10.1063/1.1754094.

[4] A. Goldstein, A. Krell, Transparent ceramics at 50: progress made and further prospects, Journal of the American Ceramic Society. 99 (2016) 3173–3197.

[5] S.F. Wang, J. Zhang, D.W. Luo, F. Gu, D.Y. Tang, Z.L. Dong, G.E.B. Tan, W.X. Que, T.S. Zhang, S. Li, L.B. Kong, Transparent ceramics: Processing, materials and applications, Progress in Solid State Chemistry. 41 (2013) 20–54. https://doi.org/10.1016/j.progsolidstchem.2012.12.002.

[6] L.B. Kong, Transparent Ceramics Materials, 2015.

[7] Z. Xiao, S. Yu, Y. Li, S. Ruan, L.B. Kong, Q. Huang, Z. Huang, K. Zhou, H. Su, Z. Yao, W. Que, Y. Liu, T. Zhang, J. Wang, P. Liu, D. Shen, M. Allix, J. Zhang, D. Tang, Materials development and potential applications of transparent ceramics: A review, Materials Science and Engineering: R: Reports. 139 (2020) 100518. https://doi.org/10.1016/j.mser.2019.100518.

[8] R. Apetz, M.P.B. Bruggen, Transparent Alumina: A Light-Scattering Model, Journal of the American Ceramic Society. 86 (2003) 480–486. https://doi.org/10.1111/j.1151-2916.2003.tb03325.x.

[9] J.G.J. Peelen, Transparent hot-pressed alumina, Ceramurgia International. 5 (1979) 115–119. https://doi.org/10.1016/0390-5519(79)90016-4.

[10] J.G.J. Peelen, R. Metselaar, Light scattering by pores in polycrystalline materials: Transmission properties of alumina, Journal of Applied Physics. 45 (1974) 216–220. https://doi.org/10.1063/1.1662961.

[11] K. Hayashi, O. Kobayashi, S. Toyoda, K. Morinaga, Transmission Optical Properties of Polycrystalline Alumina with Submicron Grains, Materials Transactions. 32 (1991) 1024–1029.

[12] A. Krell, T. Hutzler, J. Klimke, Transmission physics and consequences for materials selection, manufacturing, and applications, Journal of the European Ceramic Society. 29 (2009) 207–221. https://doi.org/10.1016/j.jeurceramsoc.2008.03.025.

[13] A. Krell, P. Blank, H. Ma, T. Hutzler, M. Nebelung, Processing of High-Density Submicrometer Al_2O_3 for New Applications, Journal of the American Ceramic Society. 86 (2003) 546–53. https://doi.org/10.1111/j.1151-2916.2003.tb03339.x.

[14] A. Goldstein, Development of a Technology for the Obtainment of Fine Grain Size, Transparent $MgAl_2O_4$ Spinel Parts, J. Ceram. Sci. Tech. (2011). https://doi.org/10.4416/JCST2010-00018.

[15] A. Goldstein, Correlation between $MgAl_2O_4$-spinel structure, processing factors and functional properties of transparent parts (progress review), Journal of the European Ceramic Society. 32 (2012) 2869–2886. https://doi.org/10.1016/j.jeurceramsoc.2012.02.051.

[16] A. Krell, J. Klimke, Effects of the homogeneity of particle coordination on solid-state sintering of transparent alumina, Journal of the American Ceramic Society. 89 (2006) 1985–1992.

[17] G.A. Kumar, M. Pokhrel, A. Martinez, D.K. Sardar, Synthesis and Upconversion Spectroscopy of Yb Er Doped M_2O_2S (M = La, Gd, Y) Phosphors, Sci Adv Mater. 4 (2012) 623–630. https://doi.org/10.1166/sam.2012.1329.

[18] R. Balda, N. Hakmeh, M. Barredo-Zuriarrain, O. Merdrignac-Conanec, S. García-Revilla, M. Arriandiaga, J. Fernández, Influence of Upconversion Processes in the Optically-Induced Inhomogeneous Thermal Behavior of Erbium-Doped Lanthanum Oxysulfide Powders, Materials. 9 (2016) 353. https://doi.org/10.3390/ma9050353.

[19] N. Hakmeh, C. Chlique, O. Merdrignac-Conanec, B. Fan, F. Cheviré, X. Zhang, X. Fan, X. Qiao, Combustion synthesis and up-conversion luminescence of La_2O_2S:Er^{3+}, Yb^{3+} nanophosphors, Journal of Solid State Chemistry. 226 (2015) 255–261. https://doi.org/10.1016/j.jssc.2015.02.015.

[20] B. Fan, C. Chlique, O. Merdrignac-Conanec, X. Zhang, X. Fan, Near-Infrared Quantum Cutting Material Er^{3+}/Yb^{3+} Doped La_2O_2S with an External Quantum Yield Higher than 100%, J. Phys. Chem. C. 116 (2012) 11652–11657. https://doi.org/10.1021/jp3016744.

[21] J. Lian, B. Wang, P. Liang, F. Liu, X. Wang, Fabrication and luminescent properties of $La_2O_2S:Eu^{3+}$ translucent ceramic by pressureless reaction sintering, Optical Materials. 36 (2014) 1049–1053. https://doi.org/10.1016/j.optmat.2014.01.024.

[22] Yu.V. Orlovskii, T.T. Basiev, K.K. Pukhov, M.V. Polyachenkova, P.P. Fedorov, O.K. Alimov, E.I. Gorokhova, V.A. Demidenko, O.A. Khristich, R.M. Zakalyukin, Oxysulfide optical ceramics doped by Nd^{3+} for one micron lasing, Journal of Luminescence. 125 (2007) 201–215. https://doi.org/10.1016/j.jlumin.2006.08.031.

[23] G. Blasse, B.C. Grabmaier, A General Introduction to Luminescent Materials, in: Luminescent Materials, Springer-Verlag Berlin Heidelberg, Berlin, 1994: pp. 1–9.

[24] Daniel C. Harris, Development of hot-pressed and chemical-vapor-deposited zinc sulfide and zinc selenide in the United States for optical windows, in: 2007. https://doi.org/10.1117/12.716808.

[25] John McCloy, International development of chemical vapor deposited zinc sulfide, in: 2007. https://doi.org/10.1117/12.717870.

[26] D.C. Harris, Materials for infrared windows and domes: properties and performance, SPIE Optical Engineering Press, Bellingham, Wash, 1999.

[27] C.B. Willingham, J. Pappis, Polycrystalline Zinc Sulfide and Zinc Selenide Articles Having Improved Optical Quality, US Patent No. 4944900, n.d.

[28] Shay Joseph, Orna Marcovitch, Ygal Yadin, Avi Steimberg, Hedva Zipin, Improved rain erosion protection for multi-spectral ZnS, in: 2005. https://doi.org/10.1117/12.603106.

[29] M. Kottaisamy, R. Jagannathan, R.P. Rao, M. Avudaithai, L.K. Srinivasan, V. Sundaram, On the Formation of Flux Grown $Y_2O_2S:Eu^{3+}$ Red Phosphor, J. Electrochem. Soc. 142 (1995) 3205–3209. https://doi.org/10.1149/1.2048714.

[30] M. Pokhrel, G.A. Kumar, D.K. Sardar, Highly efficient NIR to NIR and VIS upconversion in Er^{3+} and Yb^{3+} doped in M_2O_2S (M = Gd, La, Y), J. Mater. Chem. A. 1 (2013) 11595. https://doi.org/10.1039/c3ta12205k.

[31] M. Kottaisamy, K. Horikawa, H. Kominami, T. Aoki, N. Azuma, T. Nakamura, Y. Nakanishi, Y. Hatanaka, Synthesis and Characterization of Fine Particle Y_2O_2S:Eu Red Phosphor at Low-Voltage Excitation, Journal of The Electrochemical Society. 147 (2000) 1612–1616.

[32] L. Ozawa, Preparation of Y_2O_2S:Eu Phosphor Particles of Different Sizes by a Flux Method, J. Electrochem. Soc. 124 (1977) 413–417. https://doi.org/10.1149/1.2133314.

[33] M. Pham-Thi, A. Morell, Process Optimization and Characterization of the Red No-Mill Phosphor Y_2O_2S:Eu, J. Electrochem. Soc. 138 (1991) 5.

[34] J.W. Haynes, J.J. Brown, Preparation and Luminescence of Selected Eu^{3+}-Activated Rare Earth-Oxygen-Sulfur Compounds, Journal of The Electrochemical Society. 115 (1968) 1060. https://doi.org/10.1149/1.2410877.

[35] A.M. Pires, O.A. Serra, M.R. Davolos, Yttrium oxysulfide nanosized spherical particles doped with Yb and Er or Yb and Tm: efficient materials for up-converting phosphor technology field, Journal of Alloys and Compounds. 374 (2004) 181–184. https://doi.org/10.1016/j.jallcom.2003.11.088.

[36] K. Ikeue, T. Kawano, M. Eto, D. Zhang, M. Machida, X-ray structural study on the different redox behavior of La and Pr oxysulfates/oxysulfides, Journal of Alloys and Compounds. 451 (2008) 338–340. https://doi.org/10.1016/j.jallcom.2007.04.145.

[37] Z. Liu, X. Sun, S. Xu, J. Lian, X. Li, Z. Xiu, Q. Li, D. Huo, J.-G. Li, Tb^{3+} - and Eu^{3+} -Doped Lanthanum Oxysulfide Nanocrystals. Gelatin-Templated Synthesis and Luminescence Properties, J. Phys. Chem. C. 112 (2008) 2353–2358. https://doi.org/10.1021/jp0764687.

[38] J. Dhanaraj, M. Geethalakshmi, R. Jagannathan, T.R.N. Kutty, Eu^{3+} doped yttrium oxysulfide nanocrystals – crystallite size and luminescence transition(s), Chemical Physics Letters. (2004) 6.

[39] S.-H. Yu, Z.-H. Han, J. Yang, H.-Q. Zhao, R.-Y. Yang, Y. Xie, Y.-T. Qian, Y.-H. Zhang, Synthesis and Formation Mechanism of La_2O_2S via a Novel Solvothermal Pressure-Relief Process, Chem. Mater. 11 (1999) 192–194. https://doi.org/10.1021/cm9805469.

[40] J. Fernández, R. Balda, M. Barredo-Zuriarrain, O. Merdrignac-Conanec, N. Hakmeh, S. García-Revilla, M.A. Arriandiaga, Spectroscopic and thermal study of Er-doped oxysulfide crystal powders, Proc. SPIE. 9380 (2015) 10. https://doi.org/10.1117/12.2076963.

[41] R. Balda, N. Hakmeh, O. Merdrignac-Conanec, M.A. Arriandiaga, J. Fernández, Upconversion emission of erbium-doped lanthanum oxysulfide powders for temperature sensing, Proc. SPIE. 10100 (2017) 8. https://doi.org/10.1117/12.2252319.

[42] I. Iparraguirre, J. Azkargorta, O. Merdrignac-Conanec, M. Al-Saleh, C. Chlique, X. Zhang, R. Balda, J. Fernández, Laser action in Nd^{3+}-doped lanthanum oxysulfide powders, Opt. Express. 20 (2012) 23690. https://doi.org/10.1364/OE.20.023690.

[43] J. Rodríguez-Carvajal, Recent advances in magnetic structure determination by neutron powder diffraction, Physica B: Condensed Matter. 192 (1993) 55–69. https://doi.org/10.1016/0921-4526(93)90108-I.

[44] T. Roisnel, J. Rodriquez-Carvajal, WinPLOTR: A Windows Tool for Powder Diffraction Pattern Analysis, Mater. Sci. Forum: Eur. Powder Diffraction EPDIC7. 378–381 (2001) 118–123. https://doi.org/10.4028/www.scientific.net/MSF.378-381.118.

[45] B. Morosin, La_2O_2S structure refinement and crystal field, Acta Cryst. B. 29 (1973) 2647–2648. https://doi.org/10.1107/S0567740873007284.

[46] P. Kubelka, F. Munk, Ein Beitrag zur Optik der Farbanstriche, Z. Tech. Phys. 12 (1931) 593–601.

[47] P. Makuła, M. Pacia, W. Macyk, How To Correctly Determine the Band Gap Energy of Modified Semiconductor Photocatalysts Based on UV–Vis Spectra, J. Phys. Chem. Lett. 9 (2018) 6814–6817. https://doi.org/10.1021/acs.jpclett.8b02892.

[48] K. Niihara, R. Morena, D.P.H. Hasselman, Evaluation of KI_c of brittle solids by the indentation method with low crack-to-indent ratios, J Mater Sci Lett. 1 (1982) 13–16. https://doi.org/10.1007/BF00724706.

[49] S. Palmqvist, Method att bestamma segheten hos sproda material, sarskilt hardmetaller, Jernkontorets Ann. (1957) 300.

[50] G. Roebben, B. Bollen, A. Brebels, J. Van Humbeeck, O. Van der Biest, Impulse excitation apparatus to measure resonant frequencies, elastic moduli, and internal friction at room and high temperature, Review of Scientific Instruments. 68 (1997) 4511–4515. https://doi.org/10.1063/1.1148422.

[51] ASTM International, Standard Test Method for Dynamic Young's Modulus, Shear Modulus and Poisson's Ratio by Impulse Excitation of Vibration, ASTM E1876-01, 2006.

[52] A. Janca, K. Tereszchuk, P.F. Bernath, N.F. Zobov, S.V. Shirin, O.L. Polyansky, J. Tennyson, Emission spectrum of hot HDO below 4000 cm^{-1}, Journal of Molecular Spectroscopy. 219 (2003) 132–135. https://doi.org/10.1016/S0022-2852(03)00015-8.

[53] R. Lemus, Vibrational excitations in H_2O in the framework of a local model, Journal of Molecular Spectroscopy. 225 (2004) 73–92. https://doi.org/10.1016/j.jms.2004.02.015.

[54] R.A. Nyquist, R.O. Kagel, C. Putzig, A. Leugers, The Handbook of Infrared and Raman Spectra of Inorganic Compounds and Organic Salts, Academic Press, San Diego, CA, 1996.

[55] J.A. Capobianco, F. Vetrone, T. D'Alesio, G. Tessari, A. Speghini, M. Bettinelli, Optical spectroscopy of nanocrystalline cubic $Y_2O_3:Er^{3+}$ obtained by combustion synthesis, Phys. Chem. Chem. Phys. 2 (2000) 3203–3207. https://doi.org/10.1039/b003031g.

[56] N. Hakmeh, Elaboration et caractérisation de luminophores et céramiques optiques IR à base d'(oxy)sulfures, Rennes 1, 2014.

[57] X. Luo, W. Cao, Ethanol-assistant solution combustion method to prepare La_2O_2S:Yb,Pr nanometer phosphor, Journal of Alloys and Compounds. 460 (2008) 529–534. https://doi.org/10.1016/j.jallcom.2007.06.011.

[58] L.E. Sobon, K.A. Wickersheim, R.A. Buchanan, R.V. Alves, Growth and Properties of Lanthanum Oxysulfide Crystals, Journal of Applied Physics. 42 (1971) 3049–3053. https://doi.org/10.1063/1.1660682.

[59] S. Imanaga, S. Yokono, T. Hoshina, Cooperative absorption in Eu_2O_2S, Journal of Luminescence. 16 (1978) 77–87. https://doi.org/10.1016/0022-2313(78)90008-X.

[60] R.J. Pressley, Handbook of Lasers, Chemical Rubber Co. Press, 1971.

[61] Q. Pan, D. Yang, S. Kang, J. Qiu, G. Dong, Regulating Mid-infrared to Visible Fluorescence in Monodispersed Er^{3+}-doped La_2O_2S ($La_2O_2SO_4$) Nanocrystals by Phase Modulation, Sci Rep. 6 (2016) 37141. https://doi.org/10.1038/srep37141.

[62] J.S. McCloy, B.J. Riley, D.A. Pierce, Infrared-transparent glass ceramics: An exploratory study, Journal of Non-Crystalline Solids. 410 (2015) 160–173. https://doi.org/10.1016/j.jnoncrysol.2014.11.040.
[63] O. Merdrignac-Conanec, G. Durand, N. Hakmeh, R. Ye, X. Zhang, Sulfide Ceramics for Optics and Photonics, in: Portland, Oregon, USA, 2019.
[64] ZnSe APC American Photonics Specs, American Photonics. (n.d.). https://american-photonics.myshopify.com/pages/znse-zinc-selenide (accessed April 15, 2022).
[65] D.L. Deadmore, H.E. Sliney, Hardness Of CaF_2 And BaF_2 Solid Lubricants At 25 To 670 °C, E-3448, NAS 1.15:88979, NASA-TM-88979, 1987.
[66] P. Aubry, Elaboration de céramiqeus transparentes fluorées activées à l'Ytterbium pour application laser, Université Pierre et Marie Curie (Paris VI), 2009.
[67] G.R. Durand, Q. Bizot, N. Herbert, S. Quéméré, M. Pasturel, X. Zhang, O. Merdrignac-Conanec, Processing of $CaLa_2S_4$ infrared transparent ceramics: A comparative study of HP and FAST/SPS techniques, J Am Ceram Soc. 103 (2020) 2328–2339. https://doi.org/10.1111/jace.16918.
[68] G. Durand, Élaboration de céramiques transparentes de $CaLa_2S_4$ pour applications optiques dans l'infrarouge, Rennes 1, 2017.
[69] J.-M. Haussonne, J.L. Barton, P. Bowen, C.P. Carry, Céramiques et verres - Principes et techniques d'élaboration, Presses Polytechniques et Universitaires Romandes, 2005.
[70] M.N. Rahaman, Ceramic Processing and Sintering, 2nd Edition, Taylor & Francis, 2003.
[71] C.S. Pande, K.P. Cooper, Nanomechanics of Hall–Petch relationship in nanocrystalline materials, Progress in Materials Science. 54 (2009) 689–706. https://doi.org/10.1016/j.pmatsci.2009.03.008.
[72] D. Townsend, J.E. Field, Fracture toughness and hardness of zinc sulphide as a function of grain size, J Mater Sci. 25 (1990) 1347–1352. https://doi.org/10.1007/BF00585448.
[73] R.W. Rice, Grain size and porosity dependence of ceramic fracture energy and toughness at 22°C, Journal of Materials Science. 31 (1996) 1969–1983.
[74] W. Yao, J. Liu, T.B. Holland, L. Huang, Y. Xiong, J.M. Schoenung, A.K. Mukherjee, Grain size dependence of fracture toughness for fine grained alumina, Scripta Materialia. 65 (2011) 143–146. https://doi.org/10.1016/j.scriptamat.2011.03.032.
[75] A.O. Surendranathan, An Introduction to Ceramics and Refractories, 1st edition, CRC Press, Boca Raton, 2014.

Declaration of interests

☒ The authors declare that they have no known competing financial interests or personal relationships that could have appeared to influence the work reported in this paper.

☐The authors declare the following financial interests/personal relationships which may be considered as potential competing interests: